

Experimental Demonstration of Plasmon-Enabled Monolithic Bragg Reflectors for Infrared Light via Inverse Design

Mikołaj Badura¹, Mikołaj Janczak², Michał Rygała³, Tristan Smołka³, Adriana Łozińska¹, Wojciech Dawidowski¹, Paweł Piotr Michałowski⁴, Beata Ściana¹, Marcin Motyka³, and Tomasz Czyszanowski²

¹Faculty of Electronics, Photonics and Microsystems, Wrocław University of Science and Technology, ul. Janiszewskiego 11/17, 50-372 Wrocław, Poland

²Photonics Group, Institute of Physics, Łódź University of Technology, ul. Wolczanska 219, 93-005 Łódź, Poland

³Laboratory for Optical Spectroscopy of Nanostructures, Department of Experimental Physics, Faculty of Fundamental Problems of Technology, Wrocław University of Science and Technology, Wybrzeże Wyspiańskiego 27, 50-370 Wrocław, Poland

⁴Łukasiewicz Research Network — Institute of Microelectronics and Photonics, 02-668 Warsaw, Aleja Lotników 32/46, Poland

January 8, 2026

Abstract

High-reflectivity mirrors in the mid-infrared (MIR) range are essential for next-generation optoelectronic devices but are still constrained by strain accumulation, poor thermal conductivity, and growth instability of thick multi-alloy stacks in conventional distributed Bragg reflectors (DBRs). We introduce plasmon-enabled DBRs (PE DBRs) based on modulation-doped monolithic InP, where plasmonic dispersion in highly doped layers provides a strong refractive-index contrast. Using inverse-design optimization targeting reduced free-carrier absorption and maximized reflectivity, we demonstrate that PE DBRs can achieve reflectivities approaching 100%. Experimentally grown 14 μm thick InP PE DBRs exhibit up to 99% reflectance with bandwidths reaching 18% of the design wavelength. The monolithic, junction-free configuration ensures low resistivity and enhanced thermal performance, offering a scalable platform for efficient plasmonic mirrors in MIR photonics, with potential applications in photodetectors, light-emitting diodes and lasers.

1 Introduction

Mid-infrared optoelectronic devices have gained significant importance across various technology fields, including thermal imaging, free space communication, human-eye-safe LIDAR systems, and detection of toxic gases with strong absorption lines in the 4 to 10 μm wavelength range¹. In this range, interband cascade (IC) and quantum cascade (QC) active regions are widely employed in lasers (ICLs, QCLs)^{2,3,4}, light emitting diodes (LED)⁵, resonant cavity (RC) LEDs⁶, photodetectors (PD)⁷ and RC PDs⁸. Surface emission in lasers and LEDs offers several advantages over edge emission, such as high optical power, wafer-level testing, two-dimensional integration enabling low

beam divergence and near-Gaussian beam distribution in the far field⁹. PDs in a vertical configuration enable higher packing density, reduced footprint, increased responsivity, and low capacitance, resulting in faster response times¹⁰. For all surface emitting or detecting configurations, planar reflectors play a crucial role in their operation enhancing the quality factor of the lasers, RC LEDs, RC PDs, redirecting the light in LEDs and recycling the light in PDs.

A conventional planar reflectors of high optical power reflectance utilize distributed Bragg reflectors (DBRs) that consist of numerous half-wavelength, optical thicknesses periods. Each period of a DBR in its most common configuration consists of two layers made of different materials with distinctly different refractive indices, negligible absorption, and thicknesses corresponding to one quarter of the design wavelength. The conduction band offset between materials of different refractive indices creates a Schottky barrier at their interfaces, which hinders current flow in electrically conductive DBRs. Moreover, the interfaces between layers in DBRs reduce the heat conductivity with respect to bulk material due to modification of phonon dispersion and phonon scattering¹¹. These effects can be reduced by replacing the sharp interface between two different materials with a gradual compositional change. In such configurations, the unit block of the DBR has a half-wavelength optical thickness, and its constituent layers are no longer of quarter-wavelength thickness¹².

The epitaxial growth of semiconductor-based DBRs poses technical challenges due to mismatched lattice constants of materials with sufficiently high refractive index contrast. However prominent exception of $\text{Al}_x\text{Ga}_{1-x}\text{As}$ exhibits acceptable lattice constants matching and high refractive index contrast, making it suitable for near and mid-infrared applications¹³. Furthermore, extensive research has been conducted on alternative materials that can achieve lattice matching with other systems, such as AlGaAsSb lattice matched to InP¹⁴ or AlGaSb lattice matched to GaSb¹⁵ as well as AlInN lattice matched to GaN¹⁶ and AlInN layers matched to AlGaN both for visible spectral range¹⁷. In the case of mid-infrared devices pose an additional challenge, even for lattice-matched materials, as the required total DBR thickness to achieve high reflectivity surpasses the critical thickness of the DBR stack. Exceeding critical thickness leads to defects and mechanical instability of the wafer. Conversely, DBRs composed of dielectric materials, which are not constrained by lattice-match requirements, face limitations such as high thermal resistivity and a lack of electrical conductivity. Recently, Li et al.¹⁸ provided an alternative approach of creating monolithic and homoepitaxial InP DBRs by electrochemical porosification of periodically distributed Si doped InP layers. Manipulation of the refractive index can be achieved through porousified InP containing voids of sufficiently small dimensions, which, for infrared light, form a homogeneous region with refractive index which value is averaged by volumes of InP and air.

In the infrared spectral range, semiconductors exhibit pronounced variations in the refractive index, which originate from collective oscillations of free carriers (plasmons) induced by a time-varying electric field, as described by the classical Drude model. As will be discussed in Section 2, these plasmons lead to a decrease in the absolute value of real part of the refractive index and a substantial increase in the absolute value of imaginary part.

In this article, we utilize this variation in the complex refractive index induced by modulation of free electron concentration and propose a design for highly reflective mid-infrared DBRs using a monolithic InP structure with doping modulation, as illustrated in Fig. 1. The demonstration of the DBR with doping modulation serves as proof of concept for a broader approach, where any unitary or binary semiconductor material with modulation doping can function efficiently as a DBR for infrared light. Unlike multilayer DBR designs, this monolithic structure eliminates interface nonuniformities, stress-induced defects, and structural instabilities, thus removing the critical thickness limitation. Consequently, this configuration enables the growth of thicker layers required for IR applications and simplifies the epitaxial process by reducing the need for extensive preconditioning. Monolithic DBRs,

composed of unitary or binary materials free from interfaces between layers with different lattice constants, also exhibit enhanced thermal conductivity compared to ternary or quaternary multilayer DBRs. The absence of such interfaces, which often induce abrupt bandgap discontinuities resembling Schottky junctions, further improves electrical conductivity, approaching values characteristic of bulk materials.

The DBR configurations that we discuss in this article are referred to as plasmon-enabled (PE) DBRs, as they utilize plasmon-induced changes in the refractive index to achieve high reflectivity in the mid-infrared range. The concept of plasmon-enabled (PE) DBRs was first proposed by Bergthold et al. in¹⁹. In their study, a PE DBR configuration composed of InAsSb/GaSb was designed for operation at a central wavelength of $4.2\text{ }\mu\text{m}$. The design assumed that the thickness of the DBR layers adhered to the quarter-wavelength condition, $\lambda/(4n)$, where λ is the central wavelength and n is the real part of the refractive index of the DBR layers. This approach proved effective for wavelengths below the free carrier plasma resonance wavelength (λ_p), approximately $6\text{ }\mu\text{m}$. The optimized PE DBR achieved a maximum reflectivity of 97%.

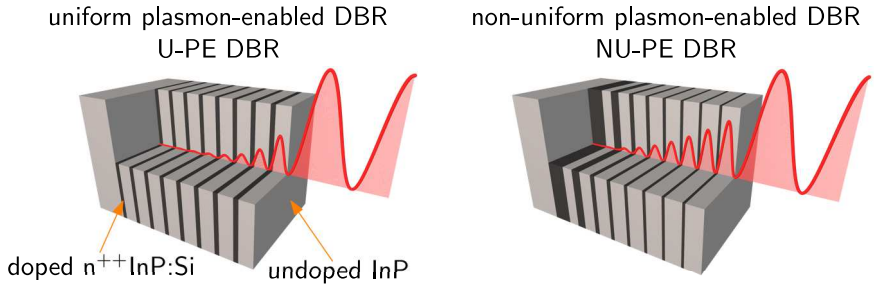


Figure 1: Cross-sectional schematics of uniform (U-) and nonuniform (NU-) plasmon-enabled (PE) DBR composed of pairs of doped (dark grey) and undoped (light grey) layers of InP, implemented on an undoped InP substrate. The red curve represents the amplitude of light incident from air. Two configurations are considered in this work: U-PE DBR with equal thicknesses of the layers in each pair, and NU-PE DBR with the thickness of the layers modified in each pair as shown in the figure.

In this article, we present an advanced approach to designing PE DBRs that goes beyond the simplistic assumption of quarter-wavelength thickness for the DBR layers. High doping layers, which create significant contrast in the complex refractive indices, enhance reflection at the interfaces between highly doped and undoped regions. However, absorption in the doped layers reduces the overall reflectivity of the PE DBR, making the design process more challenging and requiring the use of inverse-design approach. In this approach, the target optical response — in this case, maximized reflectivity and minimized absorption — is first defined, and the geometric parameters of the structure are then iteratively optimized to achieve this goal. Unlike conventional forward-design methods based on the quarter-wavelength rule, our method relies on numerical optimization of the doped and undoped layer thicknesses.

We propose two design schemes for PE DBRs. The first, referred to as the uniform PE DBR (U-PE DBR), uses identical layer thicknesses throughout each period. The second, the non-uniform PE DBR (NU-PE DBR) intentionally varies the thicknesses of the doped and undoped layers within each DBR segment to minimize absorption losses and maximize reflectivity (see Fig. 1 for schematics). We numerically demonstrate that the reflectivity of NU-PE DBRs can approach nearly 100% across a broad infrared range, including wavelengths beyond the free carrier plasma resonance. The findings of the numerical analysis are validated by the experimental realization of three InP NU-PE DBRs

targeting $\sim 5 \mu\text{m}$, $\sim 7 \mu\text{m}$, and $\sim 9 \mu\text{m}$, with the latter achieving reflectivity as high as 99.6%.

2 Reflection from highly doped uniform layer

The reflection from the interface between two layers with different complex refractive indices can be described by the Fresnel equations. For normal incidence, the optical power reflectance is given by:

$$R = \frac{(n_2 - n_1)^2 + (k_2 - k_1)^2}{(n_2 + n_1)^2 + (k_2 + k_1)^2} \quad (1)$$

where $n - ik$ denotes the complex refractive index, and the respective subscripts refer to materials 1 and 2. The formula (1) shows that differences in both the real and imaginary parts of the complex refractive index contribute to the reflection. In the mid-infrared range, the frequency of light is close to the eigenfrequency of free electrons in semiconductors, leading to a significant variation in their complex refractive index, which can be described using Drude's model. Figures 2a and 2b show the complex refractive index of InP as a function of carrier concentration for different wavelengths. Dots correspond to experimental data reported in²⁰, while the lines represent fitted dependencies according to the Drude model. Figures 3a and 3b present the complex refractive index of InP as a function of wavelength for various levels of n-type doping. It can be observed that, in accordance with the Drude model, the real part of the refractive index decreases with increasing wavelength and approaches a minimum close to zero near the plasma resonance wavelength λ_p . For wavelengths longer than λ_p , the semiconductor enters the plasmonic regime, characterized by a metal-like optical response. In this regime, the dielectric permittivity satisfies the condition $\text{Re}[\varepsilon] = \text{Re}[(n - ik)^2] < 0$.²¹. As a result, when infrared light with a wavelength exceeding λ_p is incident on a highly doped InP layer (from the air side in our example see Fig. 3c), plasmonic behavior is observed; however, a high reflectivity is achieved only for wavelengths sufficiently longer than λ_p . For sufficiently high doping levels, the reflectance can exceed 90% and saturates at approximately 95% for wavelengths well beyond λ_p . The calculations presented in Fig. 3c were performed for an infinitely thick layer of highly doped InP, but similar levels of reflectivity can be achieved for a layer of thickness greater than half the wavelength. However, at wavelengths below λ_p , the reflection is less than the level of Fresnel reflection calculated for undoped InP. The calculations of reflection from a homogeneous plasmonic layer presented in this section serve as a reference benchmark for the subsequent analyses in this work.

3 Numerical optimisation

We utilize the Plane Wave Admittance Method²² to perform numerical calculations of the optical power reflectance and light distribution in PE DBRs. To optimize the design, we combine an algorithm for calculating reflection with a multidimensional Nelder-Mead simplex algorithm^{23,24}. Our calculations assume a free carrier concentration of $2 \times 10^{19} \text{ cm}^{-3}$ in the doped layers and no free electrons in the undoped layers of the PE DBR. It should be noted that undoped InP typically exhibits a residual free carrier concentration on the order of 10^{13} – 10^{14} cm^{-3} ; this issue will be further discussed in Section 4. The dispersion of the complex refractive index follows the model depicted in Fig. 2 and 3.

In this example, we aim to optimize the configuration of the U-PE DBR composed of 25 DBR pairs to achieve maximal reflectivity at three chosen wavelengths of 5, 7, and $9 \mu\text{m}$, using the conventional quarter-wavelength-like design as a starting point. The exemplary optimization trajectories

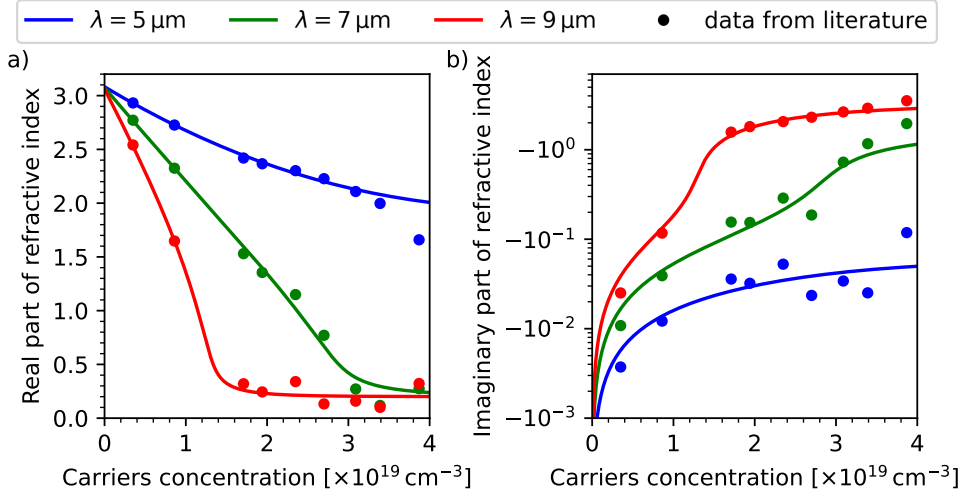


Figure 2: a) Real part and b) imaginary part of refractive index of InP. Values from²⁰ are marked by dots, lines represent dependency obtained by Drude model.

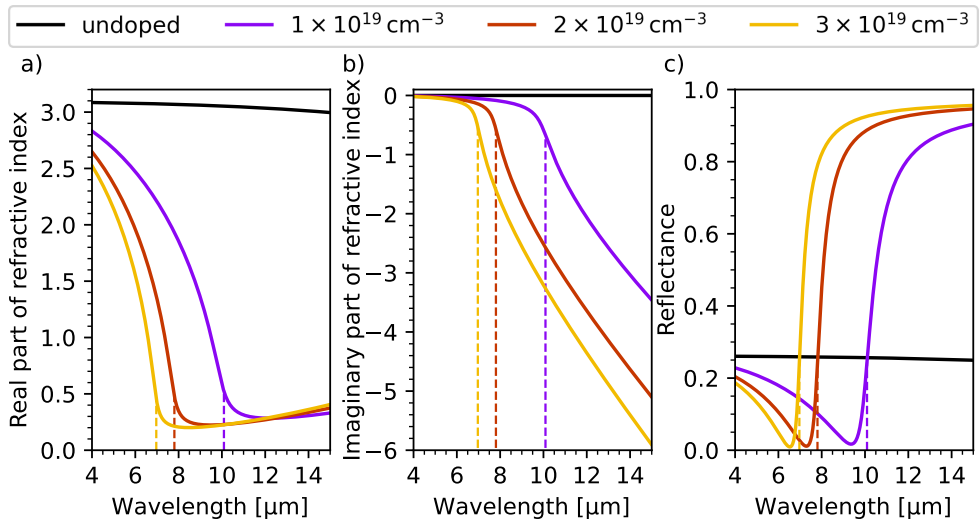


Figure 3: a) Real part and b) imaginary part of the refractive index of InP based on experimental characteristics from²⁰, and c) reflectivity of a uniform InP layer when illuminated with infrared light incident from air side, all as a function of wavelength for different levels of carrier concentration indicated by colours. Vertical dashed lines indicate plasma frequency.

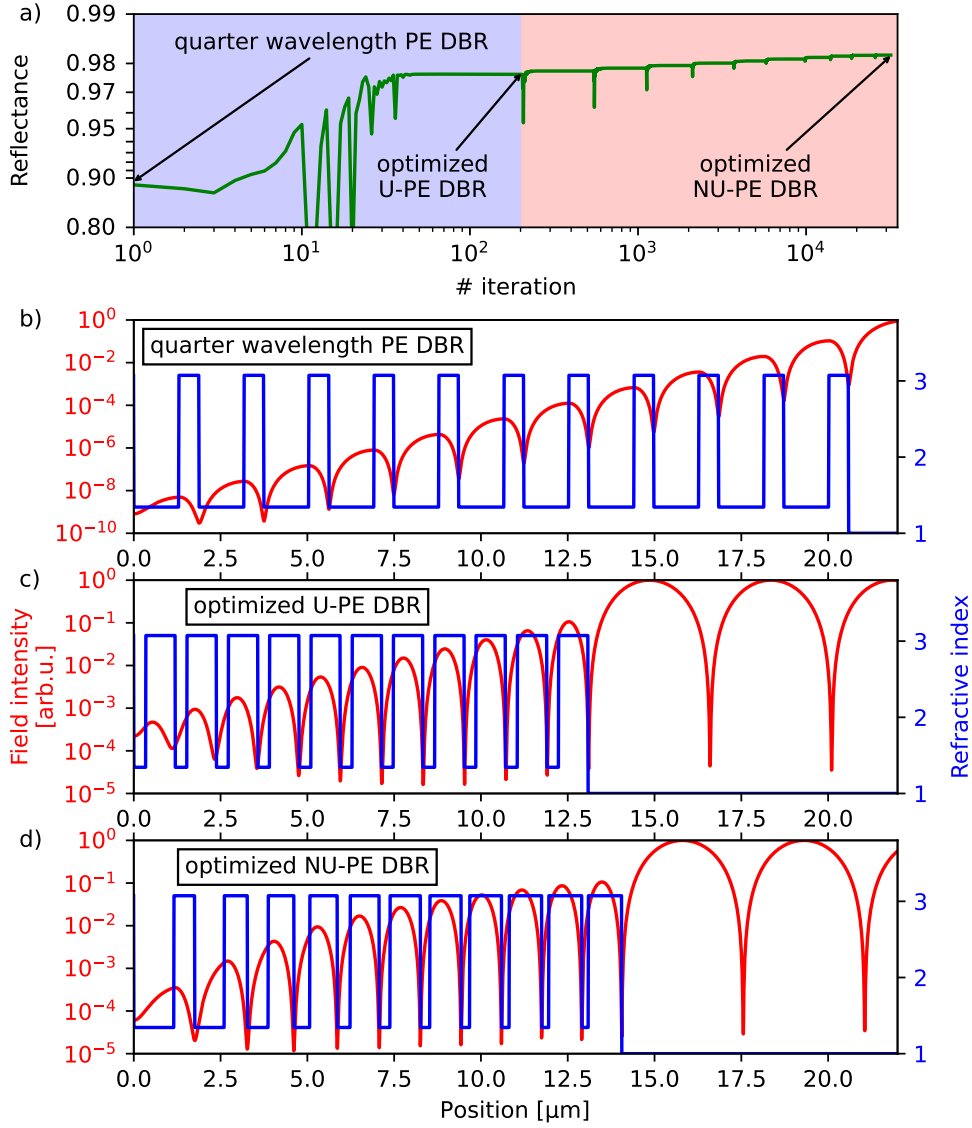


Figure 4: a) Optimisation trajectory illustrating the evolution of reflectivity at the wavelength of $7\text{ }\mu\text{m}$ for U-PE DBR and NU-PE DBR as a function of the number of iterations in the optimisation process with variable layer thicknesses. The initial PE DBR configuration assumes quarter-wavelength layer thicknesses. In the first stage (light-blue background), all DBR sections are identical, and the algorithm searches for the optimal thicknesses of the undoped and highly doped layers, resulting in the U-PE DBR design. In the second stage (light-pink background), the optimal U-PE DBR is used as the starting point, and the thickness of each individual layer is varied independently, leading to the optimised NU-PE DBR structure. Panels b), c) and d) show light intensity (red) in logarithmic scale and real refractive index (blue); b) depicts the initial PE DBR configuration, based on the quarter-wavelength layer thickness assumption, serving as the starting point for the optimization process; c) presents the U-PE DBR configuration obtained within first step of optimization procedure, d) presents the NU-PE DBR configuration obtained as the result of the optimization procedure.

of the U-PE DBR at the wavelength of $7\text{ }\mu\text{m}$, illustrated in Fig. 4a, exhibit minor decaying oscillations as the reflectivity approaches convergence, originating from successive hopping around locally optimal layer thicknesses. The transition from the initial configuration (Fig. 4b) to the optimized U-PE DBR (Fig. 4c) is driven primarily by a reduction in the thickness of the highly doped layers and their relocation toward the standing-wave node inside the DBR structure. The three optimised designs of U-PE DBR composed of 25 pairs result in reflectivities of 98.74%, 98.98%, 99.05% at the wavelengths of 5, 7, and $9\text{ }\mu\text{m}$, respectively, as shown in Figs. 5a, 5c. The layers thickness of optimal configurations are $0.600\text{ }\mu\text{m}$, **0.229** μm for $5\text{ }\mu\text{m}$, $0.941\text{ }\mu\text{m}$, **0.211** μm for $7\text{ }\mu\text{m}$ and $1.281\text{ }\mu\text{m}$, **0.201** μm for $9\text{ }\mu\text{m}$ (doped layers are in bold). Similar convergence is observed for different numbers of DBR periods. The dependence of the maximum reflectivity on the number of U-PE DBR pairs, resulting from the optimization, is shown in Fig. 5c with dashed lines. An increase in the DBR reflectance maximum increases with wavelength which is due to the increasing difference in complex refractive indices between doped and undoped layers.

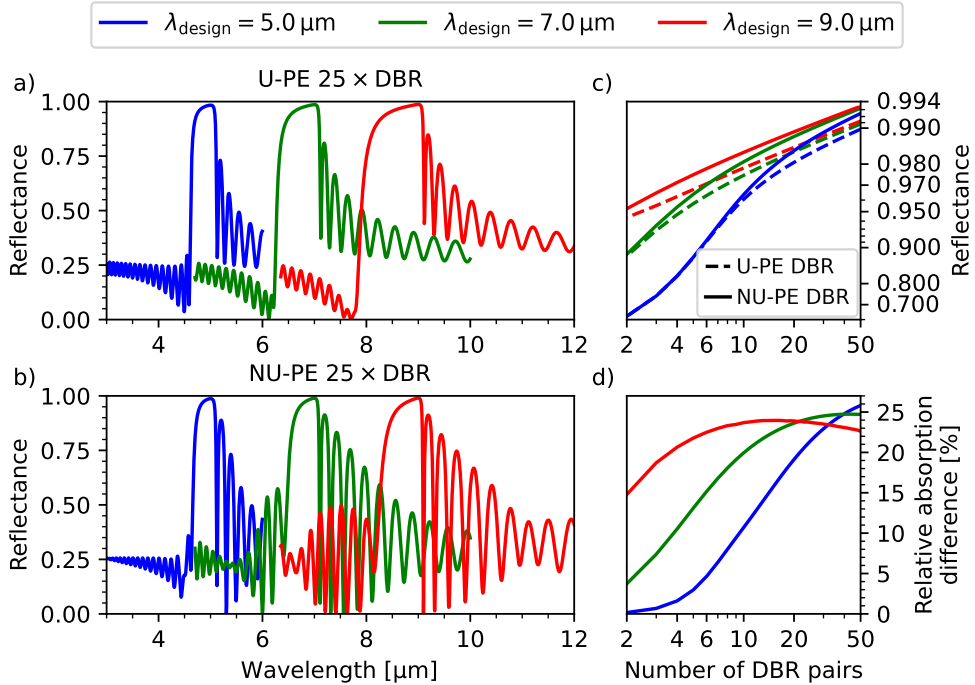


Figure 5: Calculated reflection spectra of optimised PE DBRs at the central wavelengths of 5, 7 and $9\text{ }\mu\text{m}$ indicated by different colours in the case of a) U-PE DBR and b) NU-PE DBR; c) maximal reflectance of U-PE and NU-PE DBRs designed for the various wavelengths and d) difference in relative absorption between optimised NU-PE DBR and U-PE DBR versus number of DBR sections.

In the U-PE DBR, radiation intensity decays exponentially with increasing penetration depth, causing the strongest absorption to occur in the initial layers on the light-incidence side. To reduce absorption, we introduce NU-PE DBR, in which the thickness of each layer in every pair is optimized, using the previously optimized U-PE DBR as the starting configuration. The convergence process, based on the Nelder-Mead simplex algorithm, begins from the optimized U-PE DBR point shown in Fig. 4c. The optimization yields nonlinear dependencies in the thickness of the doped and undoped layers across successive DBR sections, with the doped layers becoming progressively thicker and the undoped layers thinner for DBR sections where light intensity decreases. Interestingly, the thicknesses of the layers within successive sections do not depend on the total number of sections in

the NU-PE DBR but only on the section index itself. Consequently, for a given wavelength, there exists a unique and well-defined layer-thickness scheme that is independent of the overall number of sections composing the NU-PE DBR. As shown in Fig. 5c, the NU-PE DBRs, indicated by solid lines, exhibit higher reflectivity compared to the U-PE DBRs, demonstrating effective suppression of free-carrier absorption. This effect becomes more pronounced in NU-PE DBRs designed for longer wavelengths. Moreover, their reflectivity increases with the number of DBR pairs, approaching 100%. Figure 5b illustrates the reflection spectra of NU-PE DBRs for the design wavelengths of 5, 7, and 9 μm , which differ from U-PE DBRs, with a greater slope near the maximum reflectance and a narrower reflection stopband. The comparison of absorption in U-PE and NU-PE DBRs shown in Fig. 5d demonstrates that the NU-PE structure enables a reduction of nearly 25% in total absorption relative to the U-PE DBR. For PE DBRs with a smaller number of sections, this improvement becomes particularly pronounced at longer wavelengths, indicating a stronger beneficial impact of the NU-PE design compared to the U-PE DBR in this spectral range.

Figure 6 presents a comparison of the reflectivity of NU-PE DBRs with various configurations of conventional DBRs that could potentially be used in mid-infrared applications, plotted as a function of their total thickness. For thicknesses exceeding 10 μm , the NU-PE DBR exhibits reflectivity that becomes nearly independent of wavelength, resulting in very similar reflectance values for a given total thickness. This behavior makes the NU-PE DBR particularly well suited for longer-wavelength applications. In contrast, conventional DBRs show a much steeper increase toward 100% reflectivity; however, in their case, lattice mismatch leads to cumulative strain in thick quarter-wave layers, which causes relaxation and defect formation, rendering such geometries impractical. As a result, high-quality reflectors in these material systems at shorter wavelengths are typically implemented as ternary-composition materials²⁵, while in principle they could also be realized as short-period, strain-balanced superlattices²⁶, rather than as thick individual layers²⁷. This approach, however, would reduce the effective refractive-index contrast, necessitating thicker stacks to achieve the desired reflectivity.

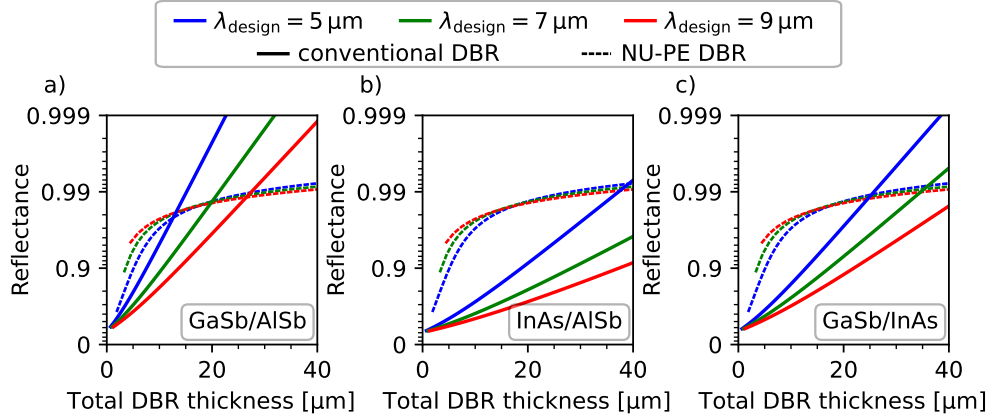


Figure 6: Calculated reflectance as a function of total DBR thickness for three design wavelengths (5 μm , 7 μm , 9 μm) for conventional quarter-wavelength: a) GaSb/AlSb DBR, b) InAs/AlSb DBR, and c) GaSb/InAs DBR. The dashed line in each panel represents the reflectance of the NU-PE DBR for comparison.

In both designs of PE DBRs, the light that is not reflected is almost completely absorbed, unlike in conventional DBRs, where the unreflected light is transmitted and only small portion of light is absorbed. Thus, the application of PE DBRs may be restricted to the role of reflecting mirrors

without the possibility of simultaneous efficient transmission. Furthermore, PE DBRs exhibit a distinct difference in their reflectance spectrum compared to conventional DBRs, as there is no clear plateau. This is attributed to the significant absorption of radiation at wavelengths different from the design wavelength of the structure.

4 Experimental characterisation

To experimentally validate the optimization results, we fabricated three NU-PE DBRs designed at wavelengths of 5, 7, and 9 μm , respectively. To maintain similar growth conditions for each NU-PE DBR, we grew the DBRs with a total thickness of approximately 14 μm , resulting in 16, 11, and 8 DBR sections designed at wavelengths of 5, 7, and 9 μm , respectively. The simulated values of peak reflectivity and the corresponding full widths at half maximum (FWHM) of the reflection spectra for the three consecutive wavelengths are presented in Table 1. The epitaxial growth of alternating $\text{n}^{++}\text{InP:Si}$ and undoped InP layers was carried out using a low-pressure metalorganic vapor phase epitaxy (LP MOCVD) system by AIXTRON with CCS 3 \times 2" FT reactor. The growth rate remained stable within the range of 1.16–1.19 nm/s, independent of both the doping concentration and the layer position. The doping concentration of $\text{n}^{++}\text{InP:Si}$ was set to $2 \times 10^{19} \text{ cm}^{-3}$, which represents the maximum level at which crystallographic defects do not compromise the interface uniformity and, consequently, the DBR reflectivity. Further increase of the doping level may be achieved by optimizing the growth temperature to suppress defect formation and mitigate the associated degradation of PE DBR reflectivity.

The growth parameters were monitored using the EpiTT LayTec *in situ* reflectometry system²⁸. The reflectometry results for the NU-PE DBR designed for 9 μm are shown in Fig. 7a. Variations in reflectivity during the growth process enables precise monitoring of the growth rates and, consequently, the determination of individual layer thicknesses. Figure 7b presents both simulated and experimental reflectivity for the growth of the second undoped InP layer, as well as the final one (Figure 7c) of the NU-PE DBR. The stable average signal level and constant oscillation period clearly indicate that the surface quality remains unchanged throughout the NU-PE DBR growth, despite the substantial total thickness of 14 μm . These results confirm that, within the homoepitaxial growth regime, the total thickness of the deposited layers does not impose a limitation that would compromise the surface morphology quality of semiconductor structures.

Figure 8 presents profiles measured using secondary ion mass spectrometry (SIMS, blue curves) and scanning capacitance microscopy (SCM, red curves) across the NU-PE DBRs designed for central wavelengths of 5 μm , 7 μm , and 9 μm . In both methods, determining the position of a given layer requires knowledge of the etching rate used in SIMS and SCM. Therefore to accurately estimate the total thickness of the DBRs, we incorporated reflectometry data, which provides the layer thicknesses in the fabricated NU-PE DBRs. SIMS reveals the intended dopant ions distribution with sharp interfaces, whereas SCM reflects the electrically active dopant profile. The smoother transitions observed in SCM between layers of different doping levels may stem from partial dopant activation or compensation effects. These discrepancies indicate that the actual electrical response deviates from the idealized sharp modulation and may therefore influence the effective complex refractive index distribution.

The reflectance spectrum of the NU-PE DBRs was measured with a Fourier transform infrared spectroscopy (FTIR) setup calibrated against a commercial gold mirror with a spot size of 250 μm . The incident light beam was directed at an angle of 13 degrees with respect to the normal direction of the sample. The reflection from the gold layer was normalized using the Fresnel equation, assuming the complex refractive index of gold from²⁹. In Fig. 9 the solid lines show the experimental reflection

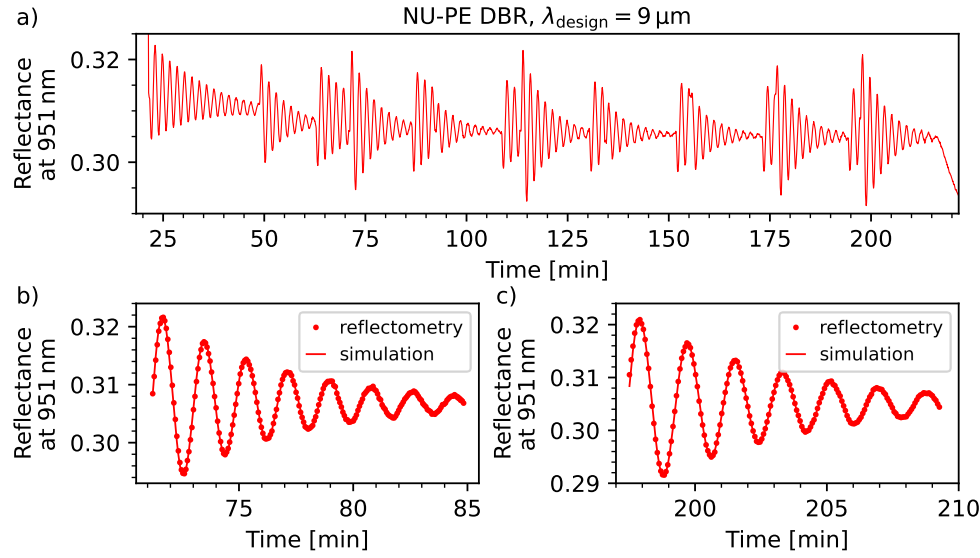


Figure 7: In-situ reflectivity at 951 nm recorded during epitaxial growth a) of the complete NU-PE DBR designed for a target wavelength of $9 \mu\text{m}$, and comparison of the reflectivity corresponding to the b) 2nd and c) 8th undoped InP layer in NU-PE DBR.

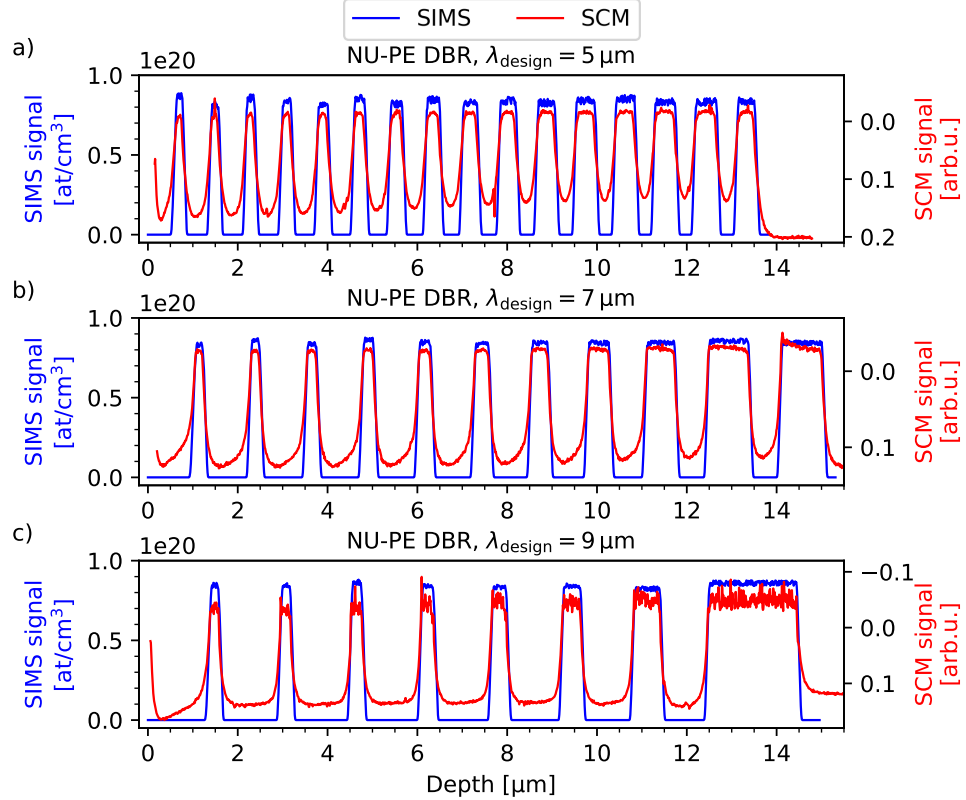


Figure 8: Secondary ion mass spectrometry (SIMS) and scanning capacitance microscopy (SCM) profiles of NU-PE DBRs designed at the wavelengths: a) 5 μm , b) 7 μm and c) 9 μm .

spectra of the NU-PE DBR samples with a stopbands centered at approximately 5, 7, and 9 μm . Maximal reflections and corresponding full-width at half maximum of the reflection spectra of fabricated samples are collected in Table 1.

Table 1: Maximum reflectivity and full width at half maximum (FWHM) of the reflection spectra obtained from numerical modelling for the designed NU-PE DBRs at incidence angles of 0° and 13° , along with experimental values measured for the fabricated NU-PE DBRs.

Design wavelength	Number of DBR pairs	theory (0°)		theory (13°)		experiment	
		Maximal reflectivity	FWHM [μm]	Maximal reflectivity	FWHM [μm]	Maximal reflectivity	FWHM [μm]
5 μm	16	98.06%	0.62	98.00%	0.61	98.98%	0.57
7 μm	11	98.22%	1.15	97.61%	1.11	93.47%	1.15
9 μm	8	98.18%	1.75	97.89%	1.73	95.20%	1.66

The dashed lines in the Fig. 9 present the calculated reflectance spectra for light incident at 13° , matching the FTIR measurement conditions. The layer thicknesses used in the simulations were taken from reflectometry results. The refractive index of heavily doped InP was calculated for a carrier concentration of $2 \times 10^{19} \text{ cm}^{-3}$, using the model shown in Fig. 2. Notably, the spectra shown in Fig. 9 were obtained without any further modification of the parameters in numerical model. A peak reflectance exceeding 90% is reproducibly achieved in the experiment, with a stopband FWHM of at least 11% of the designed wavelength. However, in the case of $\lambda = 7 \mu\text{m}$ the maximum reflectance is approximately 5% lower than the theoretically predicted value. This deviation can be attributed to several factors, including an unintentional background doping level estimated at around $7.7 \times 10^{13} \text{ cm}^{-3}$ imperfect control of high doping concentrations (confirmed by the shape of SCM profile, see Fig. 8), diffusion of free carriers into nominally undoped regions, possible deviations in layer thicknesses, and calibration uncertainty related to the absolute reflectance of the reference gold mirror.

Figure 10 visualizes the reflection properties of the NU-PE DBRs. Infrared imaging was performed using an InSb cooled infrared camera operating in the 3–5 μm spectral range (Camera 1, Fig. 10a) and a vanadium-oxide microbolometer camera sensitive in the 7.5–14 μm range (Camera 2, Fig. 10b). Both cameras image the reflection of infrared radiation from the three NU-PE DBRs discussed in this work. Radiation is emitted by an operating light-emitting diode with a surface temperature of approximately 60 $^\circ\text{C}$. Figure 10c shows the reflection spectra of the NU-PE DBRs overlaid with the normalized black-body emission spectrum at 60 $^\circ\text{C}$ and the spectral sensitivity ranges of both cameras. The strong reflected signal in Fig. 10a observed for the NU-PE DBRs designed at 5 μm (blue curve in Fig. 10c) and the 9 μm (red curve in Fig. 10e) arises from the overlap of their reflection maxima with the sensitivity band of Camera 1 (secondary reflection maximum in the case of 9 μm NU-PE DBR). In the case of the 7 μm NU-PE DBR (green curve), the thermogram is dominated by a weak radiation reflection in the Camera 1 sensitivity band. In Fig. 10b, the detected radiation intensity decreases systematically from the long-wavelength to the short-wavelength NU-PE DBRs, as the 9 μm NU-PE DBR coincides with the maximum of the black-body emission and the sensitivity range of Camera 2, while the other two NU-PE DBRs exhibit progressively weaker spectral overlap with the detector's response range.

To perform electrical characterization of the PE DBRs, transmission line measurements (TLM) were carried out on mesa structures of 9 μm NU-PE DBR defined using standard photolithography

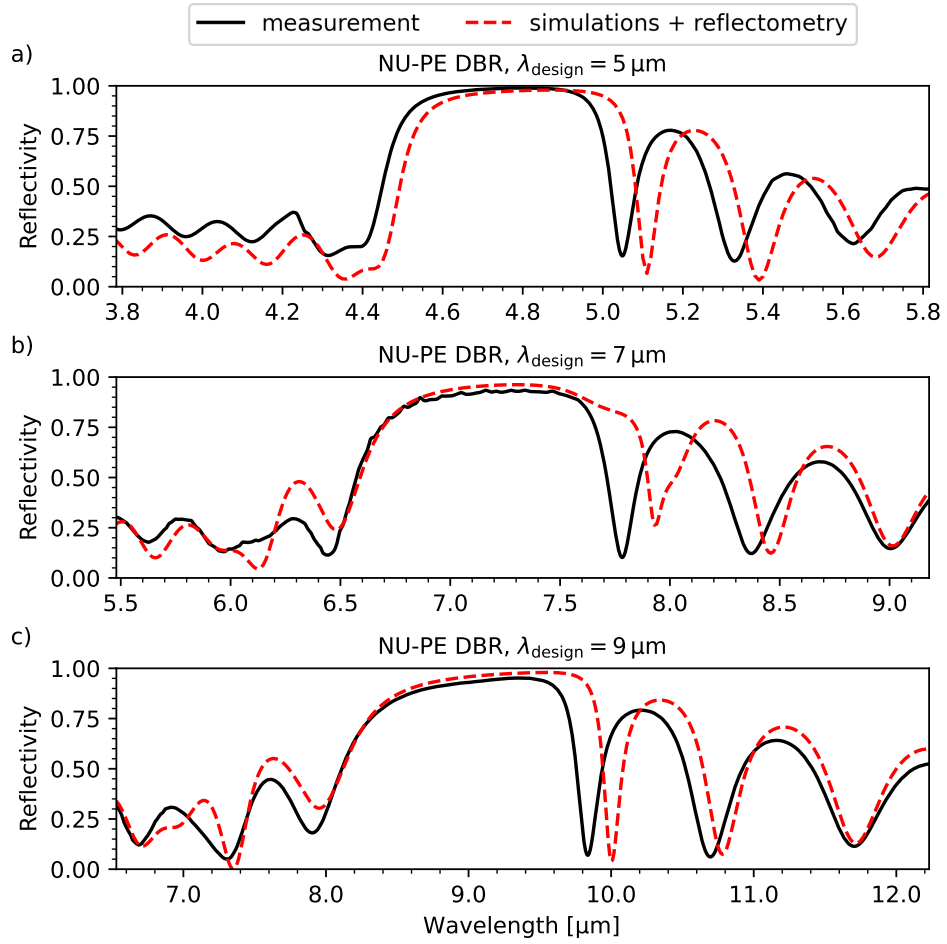


Figure 9: Measured (solid lines) and calculated (dashed lines) reflection spectra of the experimentally realized NU-PE DBRs for thicknesses of a) $5\text{ }\mu\text{m}$, b) $7\text{ }\mu\text{m}$, and c) $9\text{ }\mu\text{m}$. The layer thicknesses used in the simulations were taken from the reflectometry measurements.

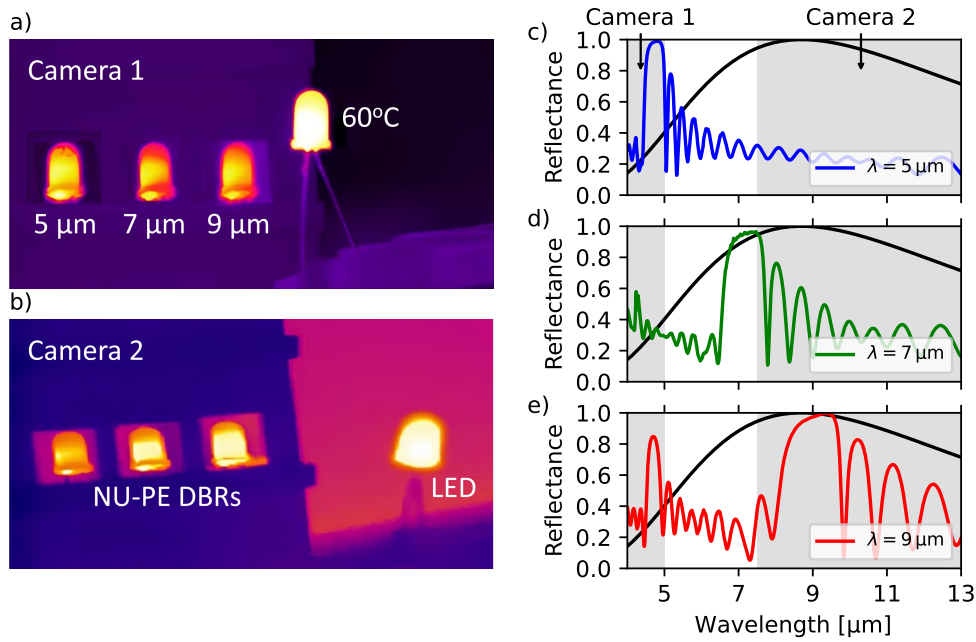


Figure 10: Infrared imaging of NU-PE DBRs illuminated by a $60\text{ }^{\circ}\text{C}$ black-body source. a) Image recorded with the InSb-cooled infrared camera ($1.5\text{--}5\text{ }\mu\text{m}$). b) Image captured with the microbolometer-based camera ($7.5\text{--}14\text{ }\mu\text{m}$). Measured reflectance spectra of the NU-PE DBRs designed for a central wavelength of a) $5\text{ }\mu\text{m}$, b) $7\text{ }\mu\text{m}$, and c) $9\text{ }\mu\text{m}$ (blue, red, and black curves, respectively), overlaid with the normalized $60\text{ }^{\circ}\text{C}$ black-body emission spectrum (black line) and the spectral sensitivity ranges of both cameras (shaded grey).

and wet chemical etching. The specific vertical resistivity of the PE DBR stack was determined to be $\sim 1.7 \Omega \text{ cm}$. This value falls between the reported low resistivity of $4 \times 10^{-4} \Omega \text{ cm}$ characteristic of highly doped n-type InP with an electron concentration of approximately $3 \times 10^{19} \text{ cm}^{-3}$ ³⁰ and the value of $11.5 \Omega \text{ cm}$ measured for intentionally undoped InP³¹. It is also comparable to, and slightly lower than, the calculated resistivities of the PE DBR stacks ($6.9 \Omega \text{ cm}$, $7.6 \Omega \text{ cm}$, $8.0 \Omega \text{ cm}$ for $5 \mu\text{m}$, $7 \mu\text{m}$, $9 \mu\text{m}$ NU-PE DBRs, respectively) obtained under the assumptions of the above-mentioned layer conductivities and the absence of resistivity-increasing effects such as junction-related barriers or carrier scattering. For reference, conventional n-type arsenide-based DBRs employing modulation doping show resistivities on the order of $10^{-3} \Omega \text{ cm}$ ³². Phosphide-based DBRs lattice-matched to InP and designed for VCSELs emitting in the $1.3\text{--}1.55 \mu\text{m}$ range exhibit resistivities of approximately $0.4 \Omega \text{ cm}$ for InP/InGaAlAs and $0.8 \Omega \text{ cm}$ for AlInAs/InGaAlAs DBRs³³, the AlP/GaP DBR implemented in a GaP-based LED demonstrates a resistivity of about $20 \Omega \text{ cm}$ ³⁴. The resistivity of the PE DBRs could be further reduced by introducing intentional doping (up to $2 \times 10^{17} \text{ cm}^{-3}$) into the originally undoped layers. This would substantially improve the electrical conductivity of the PE DBR, while only minimally affecting the refractive index contrast. Consequently, the reflectivity would slightly decrease, as is typically observed in conventional DBRs. Moreover, in a homoepitaxial PE DBR the absence of interfaces between materials with different bandgaps prevents the formation of band discontinuities and minimizes electron scattering at heterogeneous boundaries, which are inherently present in non-homoepitaxial DBRs.

5 Conclusions

We have introduced a novel plasmon-enabled distributed Bragg reflector (PE DBR) architecture for achieving high infrared reflectivity, based on modulation doping in monolithic indium phosphide. Numerical simulations combined with inverse-design optimization demonstrate that a uniform (U-PE DBR) structure composed of 50 periodic pairs of undoped and highly doped ($2 \times 10^{19} \text{ cm}^{-3}$) layers can achieve reflectivity exceeding 99% for wavelengths above $4 \mu\text{m}$. The remaining $\sim 1\%$ loss originates primarily from free-carrier absorption, which constitutes the dominant limiting factor. Furthermore, we show that this absorption can be reduced by more than 20% through the implementation of a nonuniform (NU-PE DBR) design, in which the thicknesses of all layers are independently optimized. The optimized NU-PE DBR achieves a reflectivity approaching 99.2%–99.4% for a 50-pair mirror.

To experimentally verify the performance of the inversely designed NU-PE DBRs, we fabricated homoepitaxial InP mirrors with modulated between unintentional $7.7 \times 10^{13} \text{ cm}^{-3}$ and intentional $2 \times 10^{19} \text{ cm}^{-3}$ Si doping using low-pressure metalorganic vapor phase epitaxy (MOVPE). Each NU-PE DBR, designed for central wavelengths of 5, 7, and $9 \mu\text{m}$ was grown, with a total thickness of approximately $14 \mu\text{m}$. The optical properties were characterized using Fourier-transform infrared (FTIR) spectroscopy, yielding peak reflectance values in the range of 93–99% and full-width-at-half-maximum (FWHM) bandwidths corresponding to 11–18% of the design wavelength. A detailed comparison between the simulated and measured reflectance spectra showed qualitative and quantitative agreement, confirming the predictive accuracy of the numerical model. The electrical characterization confirmed the expected behavior of the junction-free homoepitaxial configuration, moreover, the conductivity can, in principle, be modified through low-level carrier doping of the initially undoped layers. Importantly, such an approach would allow for a reduction in resistivity without significantly affecting the refractive index contrast, thereby preserving the high reflectivity of the PE DBRs. Unlike conventional DBRs, whose performance is constrained by growth time and the critical thickness imposed by strain, the plasmon-enabled DBR could provide high reflectivity

over a broader spectral range. The key advantage of plasmon-enabled DBRs lies in the ability to tailor the complex refractive index of the semiconductors through the concentration of free carriers, providing a versatile platform that can be applied to all semiconductor materials. This approach opens up new possibilities for the design and fabrication of high-performance optical devices for a variety of applications, such as lasers, optical filters, and modulators with enhanced performance and functionality.

Acknowledgements

The authors thank Fabian Hartmann (Julius-Maximilians-Universität Würzburg) for valuable discussions and support. T.C., M.M. and M.J. acknowledge financial support by the Swiss Contribution to reducing economic and social disparities in the EU and from the state budget through the National Centre for Research and Development, Call 2024/90/2025, project entitled “Quantum-cascade vertical cavity surface emitting laser for gas sensing” (QCVCSEL). This work has been completed while M.J. was the doctoral candidate in the Interdisciplinary Doctoral School at the Lodz University of Technology, Poland.

References

- [1] I. E. Gordon, L. S. Rothman, C. Hill, R. V. Kochanov, Y. Tan, P. F. Bernath, M. Birk, V. Boudon, A. Campargue, K. V. Chance, B. J. Drouin, J. M. Flaud, R. R. Gamache, J. T. Hodges, D. Jacquemart, V. I. Perevalov, A. Perrin, K. P. Shine, M. A. H. Smith, J. Tennyson, G. C. Toon, H. Tran, V. G. Tyuterev, A. Barbe, A. G. Császár, V. M. Devi, T. Furtenbacher, J. J. Harrison, J. M. Hartmann, A. Jolly, T. J. Johnson, T. Karman, I. Kleiner, A. A. Kyuberis, J. Loos, O. M. Lyulin, S. T. Massie, S. N. Mikhailyko, N. Moazzen-Ahmadi, H. S. P. Müller, O. V. Naumenko, A. V. Nikitin, O. L. Polyansky, M. Rey, M. Rotger, S. W. Sharpe, K. Sung, E. Starikova, S. A. Tashkun, J. Vander Auwera, G. Wagner, J. Wilzewski, P. Wcisło, S. Yu, and E. J. Zak. The HITRAN2016 molecular spectroscopic database. *Journal of Quantitative Spectroscopy and Radiative Transfer*, 203:3–69, December 2017.
- [2] Rui Q. Yang. Infrared laser based on intersubband transitions in quantum wells. *Superlattices and Microstructures*, 17(1):77–83, January 1995.
- [3] Jerome Faist, Federico Capasso, Deborah L. Sivco, Carlo Sirtori, Albert L. Hutchinson, and Alfred Y. Cho. Quantum Cascade Laser. *Science*, 264(5158):553–556, April 1994.
- [4] Michael Hlavatsch and Boris Mizaikoff. Advanced mid-infrared lightsources above and beyond lasers and their analytical utility. *Analytical Sciences*, 38(9):1125–1139, September 2022.
- [5] Nicolas Schäfer, Julian Scheuermann, Robert Weih, Johannes Koeth, and Sven Höfling. High efficiency mid-infrared interband cascade LEDs grown on low absorbing substrates emitting >5 mW of output power. *Optical Engineering*, 58(11):117106, November 2019.
- [6] D A Díaz-Thomas, O Stepanenko, M Bahriz, S Calvez, T Batte, C Paranthoen, G Patriarche, E Tournié, A N Baranov, G Almuneau, C Levallois, and L Cerutti. 3.3 μ m interband-cascade resonant-cavity light-emitting diode with narrow spectral emission linewidth. *Semiconductor Science and Technology*, 35(12):125029, November 2020.
- [7] Alexandare Delga. 8 - Quantum cascade detectors: A review. In *Mid-Infrared Optoelectronics*, pages 337–377. Woodhead Publishing, January 2020.

[8] Alex M. Green, David G. Gevaux, Christine Roberts, and Chris C. Phillips. Resonant-cavity-enhanced photodetectors and LEDs in the mid-infrared. *Physica E: Low-dimensional Systems and Nanostructures*, 20(3):531–535, January 2004.

[9] K. Iga. Surface-emitting laser-its birth and generation of new optoelectronics field. *IEEE Journal of Selected Topics in Quantum Electronics*, 6(6):1201–1215, November 2000.

[10] Hsuan-An Chen, Hsuan-Yu Chen, Wei-Chan Chen, and Shih-Yen Lin. Type-II Superlattice Infrared Photodetectors With Graphene Transparent Electrodes. *IEEE Photonics Technology Letters*, 29(19):1691–1694, October 2017.

[11] Kiarash Gordiz and Asegun Henry. Phonon transport at interfaces: Determining the correct modes of vibration. *Journal of Applied Physics*, 119(1):015101, January 2016.

[12] Liwen Cheng, Da Yang, and Shun Yao. Study of reflectivity and resistance properties of p-type distributed Bragg reflectors with composition graded interfaces. In *2022 International Conference on Numerical Simulation of Optoelectronic Devices (NUSOD)*, pages 71–72, September 2022.

[13] Rainer Michalzik, editor. *VCSELs: Fundamentals, Technology and Applications of Vertical-Cavity Surface-Emitting Lasers*, volume 166 of *Springer Series in Optical Sciences*. Springer, Berlin, Heidelberg, 2013.

[14] S. Nakagawa, E. Hall, G. Almuneau, J.K. Kim, D.A. Buell, H. Kroemer, and L.A. Coldren. 1.55-/spl mu/m InP-lattice-matched VCSELs with AlGaAsSb-AlAsSb DBRs. *IEEE Journal of Selected Topics in Quantum Electronics*, 7(2):224–230, March 2001.

[15] Dorian Sanchez, Laurent Cerutti, and Eric Tournié. Single-Mode Monolithic GaSb Vertical-Cavity Surface-Emitting Laser. *Optics Express*, 20(14):15540–15546, July 2012.

[16] Cleophace Seneza, Christoph Berger, Prabha Sana, Harmut Witte, Jürgen Bläsing, Anja Dempewolf, Armin Dadgar, Jürgen Christen, and André Strittmatter. Highly reflective and conductive AlInN/GaN distributed Bragg reflectors realized by Ge-doping. *Japanese Journal of Applied Physics*, 61(1):015501, December 2021.

[17] E. Feltin, J.-F. Carlin, J. Dorsaz, G. Christmann, R. Butté, M. Laügt, M. Ilegems, and N. Grandjean. Crack-free highly reflective AlInN/AlGaN Bragg mirrors for UV applications. *Applied Physics Letters*, 88(5):051108, January 2006.

[18] Bingjun Li, Chenziyi Mi, Jin-Ho Kang, Hao Li, Rami T. Elafandy, Wei-Chih Lai, Jinn-Kong Sheu, and Jung Han. Photonic engineering of InP towards homoepitaxial short-wavelength infrared VCSELs. *Optica*, 11(1):113–119, January 2024.

[19] Morgan Bergthold, Daniel Wasserman, and Aaron J. Muhowski. Plasmon-enhanced distributed Bragg reflectors. *Infrared Physics & Technology*, 125:104236, September 2022.

[20] M. E. Aryaee Panah, L. Han, K. Norrman, N. Pryds, A. Nadtochiy, A. E. Zhukov, A. V. Lavrinenko, and E. S. Semenova. Mid-IR optical properties of silicon doped InP. *Optical Materials Express*, 7(7):2260–2271, July 2017.

[21] Edoardo De Tommasi, Anna Chiara De Luca, Stefano Cabrini, Ivo Rendina, Silvia Romano, and Vito Mocella. Plasmon-like surface states in negative refractive index photonic crystals. *Applied Physics Letters*, 102(8):081113, 02 2013.

[22] Maciej Dems, Rafal Kotynski, and Krassimir Panajotov. PlaneWave Admittance Method — a novel approach for determining the electromagnetic modes in photonic structures. *Optics Express*, 13(9):3196–3207, May 2005.

[23] J. A. Nelder and R. Mead. A Simplex Method for Function Minimization. *The Computer Journal*, 7(4):308–313, January 1965.

[24] Margaret H. Wright. Direct Search Methods: Once Scorned, Now Respectable. In *Numerical Analysis 1995: Proceedings of the 1995 Dundee Biennial Conference in Numerical Analysis*, pages 191–208. Addison Wesley Longman, Harlow, UK, 1996.

[25] Dorian Sanchez, Laurent Cerutti, and Eric Tournié. Mid-IR GaSb-based monolithic vertical-cavity surface-emitting lasers. *Journal of Physics D: Applied Physics*, 46(49):495101, November 2013.

[26] Michał Marchewka, Dawid Jarosz, Marta Ruszała, Anna Juś, Piotr Krzeminiński, Dariusz Płoch, Kinga Maś, Renata Wojnarowska-Nowak, Michał Marchewka, Dawid Jarosz, Marta Ruszała, Anna Juś, Piotr Krzeminiński, Dariusz Płoch, Kinga Maś, and Renata Wojnarowska-Nowak. Strain-Balanced InAs/AlSb Type-II Superlattice Structures Growth on GaSb Substrate by Molecular Beam Epitaxy. *Materials*, 16(5), February 2023.

[27] H.-J. Gossmann, B. A. Davidson, G. J. Gaultieri, G. P. Schwartz, A. T. Macrander, S. E. Slusky, M. H. Grabow, and W. A. Sunder. Critical layer thickness and strain relaxation measurements in GaSb(001)/AlSb structures. *Journal of Applied Physics*, 66(4):1687–1694, August 1989.

[28] Resources. <https://laytec.de/resources>.

[29] Mark A. Ordal, Robert J. Bell, Ralph W. Alexander, Larry L. Long, and Marvin R. Querry. Optical properties of Au, Ni, and Pb at submillimeter wavelengths. *Applied Optics*, Vol. 26, Issue 4, pp. 744-752, February 1987.

[30] D. Pasquariello, E.S. BJORLIN, D. Lasaosa, Yi.-J. Chiu, J. Piprek, and J.E. Bowers. Selective undercut etching of InGaAs and InGaAsP quantum wells for improved performance of long-wavelength optoelectronic devices. *Journal of Lightwave Technology*, 24(3):1470–1477, March 2006.

[31] Mikołaj Badura. MOVPE Technology of Fe-Compensated In PLayers for the Quantum Cascade Laser Applications. *International Journal of Electronics and Telecommunications*; 2020; vol. 66; No 2; 389-394, 2020.

[32] Zhenyu Wen, Jianjun Li, Hongkang Cao, Jun Wang, and Xiaoqian Wang. Low series resistance N-type AlGaAs/AlAs distributed Bragg reflector grown by MOCVD. In *2019 International Conference on Optical Instruments and Technology: Micro/Nano Photonics: Materials and Devices*, volume 11440, pages 58–63. SPIE, March 2020.

[33] T. C. Lu, J. Y. Tsai, H. C. Kuo, and S. C. Wang. Comparisons of InP/InGaAlAs and In-AlAs/InGaAlAs distributed Bragg reflectors grown by metalorganic chemical vapor deposition. *Materials Science and Engineering: B*, 107(1):66–69, February 2004.

[34] Karine Hestroffer, Dennis Sperlich, Shabnam Dadgostar, Christian Golz, Jannis Krumland, William Ted Masselink, and Fariba Hatami. Transport properties of doped AlP for the development of conductive AlP/GaP distributed Bragg reflectors and their integration into light-emitting diodes. *Applied Physics Letters*, 112(19):192107, May 2018.